

# Journal of Biomedical Optics

BiomedicalOptics.SPIEDigitalLibrary.org

## **Laser cutting of bone tissue under bulk water with a pulsed ps-laser at 532 nm**

Cristian-Alexander Tulea  
Jan Caron  
Nils Gehlich  
Achim Lenenbach  
Reinhard Noll  
Peter Loosen

# Laser cutting of bone tissue under bulk water with a pulsed ps-laser at 532 nm

Cristian-Alexander Tulea,<sup>a,\*</sup> Jan Caron,<sup>a</sup> Nils Gehlich,<sup>a</sup> Achim Lenenbach,<sup>a</sup> Reinhard Noll,<sup>a</sup> and Peter Loosen<sup>a,b</sup>

<sup>a</sup>Fraunhofer Institute for Laser Technology ILT, Steinbachstraße 15, Aachen 52074, Germany

<sup>b</sup>RWTH Aachen University, Chair for Technology of Optical Systems, Steinbachstraße 15, Aachen 52074, Germany

**Abstract.** Hard-tissue ablation was already investigated for a broad variety of pulsed laser systems, which cover almost the entire range of available wavelengths and pulse parameters. Most effective in hard-tissue ablation are Er:YAG and CO<sub>2</sub> lasers, both utilizing the effect of absorption of infrared wavelengths by water and so-called explosive vaporization, when a thin water film or water–air spray is supplied. The typical flow rates and the water layer thicknesses are too low for surgical applications where bleeding occurs and wound flushing is necessary. We studied a 20 W ps-laser with 532 nm wavelength and a pulse energy of 1 mJ to effectively ablate bones that are submerged 14 mm under water. For these laser parameters, the plasma-mediated ablation mechanism is dominant. Simulations based on the blow-off model predict the cut depth and cross-sectional shape of the incision. The model is modified considering the cross section of the Gaussian beam, the incident angle, and reflections. The ablation rate amounts to 0.2 mm<sup>3</sup>/s, corresponding to an increase by at least 50% of the highest values published so far for ultrashort laser ablation of hard tissue. © 2015 Society of Photo-Optical Instrumentation Engineers (SPIE) [DOI: 10.1117/1.JBO.20.10.105007]

Keywords: ablation rate; bone tissue; water; osteotomy; ps-laser; plasma; blow-off model.

Paper 150334RR received May 17, 2015; accepted for publication Sep. 11, 2015; published online Oct. 15, 2015.

## 1 Introduction

The utilization of various laser systems with different parameters to ablate hard tissue reflects the development history and availability of such laser systems. The first investigations on hard tissue response to laser irradiation were made in the 1960s soon after the invention of the ruby laser.<sup>1</sup> In order to successfully replace mechanical burrs and saws in bone surgery, two key challenges must be overcome. First, the thermal damage induced by laser radiation to the bone tissue must be avoided, because this would lead to delayed healing.<sup>2</sup> Second, the cutting speed, which depends on the ablation rate, must be at the same level as for mechanical cutting tools. Up to now, a broad variety of laser parameters have been tested to overcome these two challenges. Efficient cutting of hard tissues such as cortical bone, dentin, or enamel has been shown with pulsed laser systems covering wavelengths from 355 nm to 10.6 μm, pulse durations from 95 fs to 300 μs, pulse energies from 10 μJ to 2 J, and average output powers from 100 mW to 100 W.<sup>3–16</sup> Most authors agree that for an efficient ablation, the laser wavelength should match the absorption bands of the tissue components or water, respectively.<sup>17</sup>

The most efficient laser systems for cutting hard tissue are the Er:YAG laser, achieving an ablation rate of  $dV/dt = 1.5 \text{ mm}^3/\text{s}$ , and the CO<sub>2</sub> laser with ablation rates of up to 3.4 mm<sup>3</sup>/s. The ablation rates given above were calculated from the ablation volumes and the specific energy given in the publications from Stock et al.<sup>18</sup> and Werner et al.<sup>19</sup> Both laser systems have pulse durations in the microsecond range and make use of the strong absorption of water at the laser wavelengths

2.94 and 10.6 μm, respectively. This absorption leads to so-called explosive evaporation of the liquid enclosed in the tissue and local disruption of the tissue. Further promising results of damage-free bone ablation were achieved with the recently developed picosecond infrared laser emitting at the Er:YAG wavelength.<sup>20</sup>

For infrared laser systems, the application of an additional liquid layer with about 1-mm thickness by a water spray with flow rates of less than 6 mL/min is needed. The purposes are first to assist the disruption effect and second to prevent heating of the tissue. The influence of such a water spray on the ablation rate is given by Stock et al.<sup>21</sup> for Er:YAG lasers and Zhang et al.<sup>22</sup> for CO<sub>2</sub> lasers. The influences of bleedings, of higher flow rates and water layers above 1 mm have to be taken into account, when laser ablation is used in surgery. For Er:YAG lasers, a drop of the ablation rate would be expected.<sup>21</sup> But for Nd:YAG lasers, the ablation rates for specimens submerged several millimeters under water are significantly higher than for ablation under dry conditions.<sup>23,24</sup>

Despite the undoubted effectiveness of the Er:YAG and CO<sub>2</sub> lasers for hard-tissue ablation, up to now, only the Er:YAG laser entered clinical routine in dentistry.<sup>25</sup> To the best of our knowledge, there is still no laser system that could replace mechanical tools for high-speed and high-volume ablation of bones, e.g., in osteotomy, craniotomy, spine surgery, or craniomaxillofacial surgery. One reason might be the drop of the ablation rate for Er:YAG lasers, when higher flow rates are needed or bleeding occurs. Another reason could be the need of deeper cuts in osteotomy than in dentistry.

A contraindication for the usage of infrared lasers with μs pulse lengths could be the results of *in vivo* studies that

\*Address all correspondence to: Cristian-Alexander Tulea, E-mail: [cristian.tulea@ilt.fraunhofer.de](mailto:cristian.tulea@ilt.fraunhofer.de)

found detrimental effects on healing. Investigations on this topic are summarized by Kuttenger et al.<sup>26</sup> According to Kuttenger et al.,<sup>26</sup> even though in some cases unimpaired wound healing after Er:YAG laser osteotomy was found, further osteotomies showed delayed healing.

Yet the most challenging tasks are to avoid thermal damage and to simultaneously achieve sufficiently high ablation rates above 1 mm<sup>3</sup>/s.

Clean and well-defined tissue removal without thermal damage can be achieved with ultrashort pulsed lasers (USPL) by means of plasma-mediated ablation.<sup>27</sup> For ablation with such laser systems, reduced collateral damage to adjacent tissue and a significant reduction of healing times below the values for cutting with mechanical drills have been observed.<sup>28</sup> However, the ablation efficiencies are one order of magnitude lower than for a thermal ablation process. The highest ablation rates achieved with USPL on hard tissue without thermal damage are 0.13 ± 0.02 mm<sup>3</sup>/s in mammoth ivory and 0.10 ± 0.05 mm<sup>3</sup>/s in dental enamel.<sup>16</sup> Even for plasma-mediated ablation, tissue can heat up to the melting point because of the thermal energy transfer from the plasma to the tissue or heat accumulation at high-repetition frequencies.<sup>29</sup>

For subnanosecond pulse durations, the ablation is no longer based on thermal interaction. Using USPL, two ablation processes take place in connection with a laser-induced breakdown. The first is the plasma-mediated ablation, which is caused by ionization of bone material and adjacent water. Sometimes, plasma-mediated ablation is also referred to as plasma-induced ablation. The second one is called photodisruption and is caused by shock waves, high pressures, and tensile forces. Both ablation processes are relatively independent of the initial absorption coefficient of the tissue, because of the prevailing nonlinear absorption features.<sup>30</sup> Therefore, water absorption bands in the infrared region no longer play a role, hence any other wavelengths, e.g., visible and ultraviolet wavelengths, come into consideration.

In summary, USPL perform ablation with lower rates than lasers with microsecond pulse lengths, such as Er:YAG or CO<sub>2</sub> lasers, despite the fact that the conversion efficiency of light energy into mechanical energy for plasma-mediated ablation is larger than for any other laser material interaction.<sup>31</sup> The potential for nonthermal, efficient cutting of hard tissue has not been exhausted yet, and the investigation of ps- and fs-lasers for hard-tissue ablation remains a challenge. In clinical practice of bone treatment with USPL, only stapedotomy has been established so far.<sup>25</sup>

## 2 Selection of Appropriate Laser Parameters

The ablation efficiency of a plasma-mediated process depends on several laser parameters, such as the wavelength  $\lambda$ , the pulse energy  $E_p$  and the pulse duration  $\tau_p$ . Therefore, these parameters have to be examined thoroughly with regard to the ablation mechanisms and side effects during plasma-mediated ablation.

First of all, a laser wavelength should be chosen, for which the ambient medium has low absorption, in order to minimize energy loss in the optical path toward the processing region. The absorption coefficient of water is given by Hale and Querry.<sup>32</sup> It is lowest in the wavelength range from the near UV to the near IR. For a typical fundamental laser wavelength of 1064 nm, the transmission through 14 mm of water amounts to 80%. For lower wavelengths down to 355 nm, the transmission increases to values greater than 99.5%. With regard to maximum energy

deposition in the target, the greater transmission can be balanced out by the conversion efficiency to generate 532 and 355 nm radiation. A typical conversion efficiency for second-harmonic generation is below 70%, while for third-harmonic generation (THG) it amounts to 30%.<sup>33</sup> Due to the low conversion efficiency of the THG and the absorption dependent thermally induced lens that leads to defocussing when using 1064 nm,<sup>34</sup> 532 nm is expected to lead to maximum ablation.

The second parameter of crucial importance is the pulse energy  $E_p$  which is directly proportional to the fluence  $F$  for a given beam waist. For a plasma-mediated ablation, a logarithmic dependence of the ablated depth per pulse  $D$  on the ratio  $\beta = F/F_{\text{thr}}$  was derived for dielectrics by Gamaly et al.,<sup>35</sup> and for metals by Nolte et al.<sup>36</sup> according to

$$D = \mu \ln(\beta). \quad (1)$$

Here,  $\mu$  is the thickness of the so-called skin layer, which is correlated to the thermal or optical penetration depth, depending on which one is larger. Assuming this dependence, according to Vogel et al.<sup>37</sup> [Fig. 33(a)], the pulse energy should be 2.5 to 5 times the threshold value, in order to achieve maximum ablation efficiency.

The third parameter of crucial importance is the pulse duration  $\tau_p$ . As a first approximation, the pulse duration should be as short as possible in order to minimize heat diffusion during the laser pulse. However, the threshold irradiance strongly depends on the pulse duration and rises for decreasing pulse durations from 10<sup>10</sup> W/cm<sup>2</sup> for ns-pulses to 10<sup>13</sup> W/cm<sup>2</sup> for fs-pulses.<sup>38</sup> Considering only the threshold condition, ns-pulses should be the best choice. Yet, light absorption and reflection by the plasma created on the tissue surface, the so-called plasma shielding must be considered, which depends on pulse duration and the wavelength.<sup>27</sup> When the laser beam provides an energy in excess of the breakdown threshold, the plasma extends during the laser pulse toward the incoming beam and largely reduces the amount of laser light reaching the target.<sup>39</sup> Therefore, laser parameters should be chosen for which the transmission through the plasma is maximal. The values of transmission through the plasma from Nahen and Vogel<sup>40</sup> are calculated for plasmas formed in distilled water. These values are a first-order approach for plasma shielding, although the plasma is formed on the bone surface. The transmission is highest for pulse durations between 1 and 100 ps and lower for visible than for infrared wavelengths. It is also highest at the threshold and drops exponentially for higher energies.

Taking into account the results of the cited references in Sec. 1, the achievable ablation rate scales with the average laser output power regardless of the microscopic ablation process. For fixed pulse energy, the average laser power is proportional to the repetition frequency  $f_R$  of the laser system. The repetition frequency should be chosen as high as possible, as long as the scanning speed can be increased likewise, in order to avoid an unnecessary heat accumulation.<sup>37</sup>

## 3 Simulation of Cutting Macroscopic Incisions

Most of the ablation models require an exact knowledge of the thermal and optical material properties. These properties are measured under physiological conditions. However, irradiating high-laser intensities can lead to significant changes of these material "constants."<sup>41</sup>

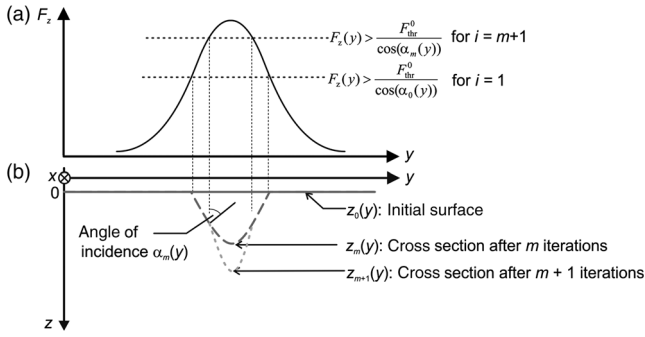


**Fig. 1** Simulation of the ablation cross section by a sequence of laser pulses with an ideal Gaussian beam profile: (a) the fluence and (b) the surface position. The dashed lines illustrate the evolving crater cross sections after  $m$  and  $m + 1$  iterations.

For the plasma-mediated process, an ablation depth per pulse according to Eq. (1) is predicted. The same equation is given by the blow-off model, which is independent of the primary ablation process.<sup>42</sup> In Eq. (1), the coefficient  $\mu$  and the threshold fluence  $F_{\text{th}}$  must be known. This equation contains no dependence of the depth  $D$  on the number of pulses  $m$ . Hence the total depth  $z_m$  should increase linearly with  $m$ . This is in contradiction to our experimental observations.

In this section, we will amend the equation in order to predict the total ablation depth and the cross-sectional shape for macroscopic incisions that are produced by laser scanning. We consider the spatial Gaussian distribution of the laser irradiance and reflections at the steep incision walls.

The calculation of the ablation depth for consecutive laser pulses with a Gaussian beam profile at a certain position on the tissue surface is illustrated in Fig. 1, while the calculations for a macroscopic incision performed by a raster scan are shown in Fig. 2. The initial tissue surface is located in the  $xy$ -plane, and the propagation direction of the laser beam is along the positive  $z$ -axis. The ablation by the scanned sequence of the laser pulses is calculated consecutively for each line number.

For a strong scattering tissue like bone,<sup>43</sup> losses due to diffuse reflection at the steep walls can occur. Therefore, the absorbed amount of energy leading to ablation is reduced. For the sake of simplicity, we assume that the total amount of reflected light can be estimated in a first-order approach by Fresnel's equation using a mean value for both polarizations and a refractive index of  $n = 1.5$  for bone<sup>44</sup> and  $n = 1.33$  for water.<sup>32</sup>

The effective fluence for an incident Gaussian beam with an incident angle  $\alpha$ , cf. Fig. 1, is given by

$$F_{\text{eff}}[y, x = x_j, \alpha(y)] = F_0 \exp\left[\frac{-2(y - y_{\text{pulse},k})^2}{w_{\text{ts}}^2}\right] \times [1 - R(\alpha(y)) \cos[\alpha(y)]], \quad (2)$$

where  $F_0 = 2E_p / \pi w_{\text{ts}}^2$  is the maximum peak fluence,  $y_{\text{pulse},k}$  is the center position of the laser pulse in line  $k$  of the raster scan shown in Fig. 2, and  $w_{\text{ts}}$  is the beam radius on the tissue surface. Here, we simplify that  $F_0$  is constant for all  $x$ -positions, which is equivalent to a pure two-dimensional (2-D) approach restricted to the  $yz$ -plane. The beam radius  $w_{\text{ts}}$  used in the calculations is an effective beam radius of an ideal Gaussian beam corresponding to the same fluence as an elliptical beam used in the experiment. The surface position is  $z$  and  $R$  is the reflected portion of the light. Here, we assume that the focus is shifted after each ablated layer according to the ablated depth, i.e.,  $w_{\text{ts}} = \text{const}$ .

To calculate the pulse energy  $E_p$  in Eq. (2), we take into account that 12% are lost along the optical path due to absorption and reflection by the optical elements. Furthermore, we assume that the amount of energy that is absorbed in the plasma is 15% for our laser parameters, according to Ref. 40. That leads to  $E_p = (1 - 0.15)(1 - 0.12)P_L / f_R$ , where  $P_L$  is the laser radiant flux measured at the exit aperture of the laser system and  $f_R$  is the pulse repetition rate.

For the simulations, we use the following input parameters:  $P_L = (20 \pm 0.1)$  W,  $f_R = 20$  kHz, beam radius at the tissue surface  $w_{\text{ts}} = (120 \pm 40)$   $\mu\text{m}$ , as measured and described in Sec. 4.

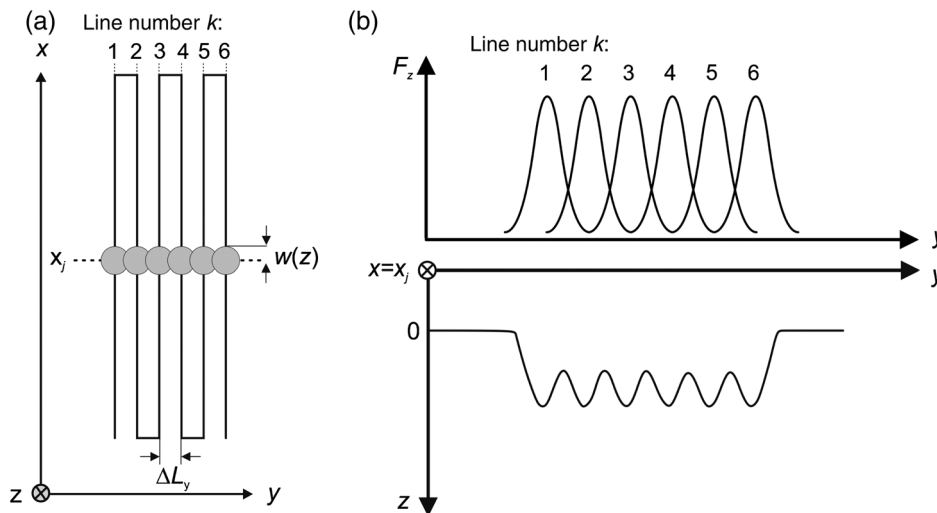


**Fig. 2** (a) Rectangular raster scan in the  $xy$ -plane. The dashed line indicates the position  $x_j$  where the surface position and groove depth is calculated. The circles indicate the center positions  $y_{\text{pulse},k}$  of the pulses with Gaussian intensity distribution and a beam radius  $w(z)$  with respect to the line distance  $\Delta L_y$ . (b) Simulated fluence for consecutive scan lines along the cross section at  $x = x_j$  and calculated ablation depth. The shown incision cross section is an exaggerated illustration.

The calculation of the ablated depth at each point  $y$  is illustrated in Fig. 1. The depth is calculated in an iterative way for the  $m$ 'th ablated layer after  $i = m$  iterations, starting with a flat surface at the position  $z_0(y) = 0$  and adding at each position  $y$ , the depth created by a pulse according to  $z_m(y) = z_{m-1}(y) + D[y, \alpha(y)]$ , with

$$D[y, \alpha(y)] = \begin{cases} \mu \cdot \ln \left\{ \frac{F_{\text{eff}}[y, \alpha(y)]}{F_{\text{thr}}^0} \right\} & \text{for } F_{\text{eff}} \geq F_{\text{thr}}^0 \\ 0 & \text{else} \end{cases} \quad (3)$$

The threshold fluence was determined from ablation experiments, where either the beam radius or the pulse energy was varied until no ablation occurred. A further method to determine the threshold was used, the so-called  $D^2$ -method described by Emigh et al.<sup>45</sup> The values from all experiments range from  $F_{\text{thr}} = 0.3 \text{ J/cm}^2$  to  $1.5 \text{ J/cm}^2$ . Within this range,  $F_{\text{thr}}$  is a free parameter in the simulation. Also unknown is the coefficient  $\mu$ . A good guess for a start value is given by Nolte et al.,<sup>36</sup> where the skin layer depth is in the order of  $0.1 \mu\text{m}$ .

## 4 Experimental Setup for *In Vitro* Studies

### 4.1 Preparation of Specimens

Fresh cortical femur bones from slaughtered cows were cut into pieces of  $2 \times 3 \times 0.5 \text{ cm}^3$  using a bandsaw. The periosteum and adherent fat was removed with a scalpel. The surface of the bones was left unpolished. A first group of samples had been stored at  $-18^\circ\text{C}$  until 1 hour prior to the ablation experiments. Another group of samples were kept at room temperature. A further group of samples was fixed histologically in formalin after they had been bought from the slaughter. For the ablation experiments, the bone samples were put in the water-filled sample chamber. In our experiments, we observed no differences in the ablation rate between the fixed samples, the defrosted samples, and the samples kept at room temperature.

### 4.2 Laser System

Based on the considerations described in Sec. 2, we used a Nd:YVO<sub>4</sub> laser system based on the innoslab amplifier.<sup>46</sup> The laser provides frequency-doubled pulses of a wavelength of 532 nm with 25 ps pulse duration at repetition frequencies up to 100 kHz. The maximum pulse energy is  $E_p = (1.4 \pm 0.01) \text{ mJ}$  at 1 kHz and the maximum output radiant flux is  $P_m = (20 \pm 0.1) \text{ W}$  for 20 kHz, measured with a thermal detector (LM45, Coherent Inc., Santa Clara, California). The beam radius was measured with a beam analyzer (M2-200-FW-BB, Ophir-Spiricon, Utah). The elliptical and astigmatic laser beam has half diameters of  $w_{x,0} = (1.3 \pm 0.5) \text{ mm}$  and  $w_{y,0} = (1.6 \pm 0.7) \text{ mm}$  at the position of the focusing lens.

### 4.3 Ablation Setup

The experimental setup is shown in Fig. 3. The bones were placed in a water-filled chamber (see Fig. 4). The laser beam deflection on the tissue surface was performed by a 2-D galvanometer scanner (IntelliSCAN 14, Scanlab AG, Puchheim, Germany) and the focus shift after each ablation layer was performed by a Galilean telescope (VarioSCAN, Scanlab AG, Puchheim, Germany). The beam was focused by a f-theta-lens with a focal length of 163 mm. The beam radius was measured in air with the CCD-camera of the beam analyzer in the focal plane and along the optical axis 12 mm above and beyond the focal plane. The Rayleigh length of the beam was  $z_R = (0.81 \pm 0.2) \text{ mm}$ . The focusing half angle of the laser beam is  $\theta_D = (20.3 \pm 1.2) \text{ mrad}$ .

The shift of the focal position in the water-filled chamber was calculated with the equation  $l_{f,w} = n_w l_{f,a}$ . Here,  $l_{f,a} = 14 \text{ mm}$  is the distance from the downside of the antireflection coated window to the focal plane for an air-filled sample chamber. With the refractive index of water for green light  $n_w = 1.33$ , the focus was shifted by 4.6 mm into the bone sample. The Rayleigh length in water is increased by the factor  $n_w^2$  to  $z_{R,w} = (1.4 \pm 0.35) \text{ mm}$ . The effective beam radius on the tissue surface was  $w_{ts} = (120 \pm 40) \mu\text{m}$ . For 1 mJ pulse energy, this corresponds to a fluence of  $F = (2.21 \pm 0.03) \text{ J/cm}^2$ , which is five

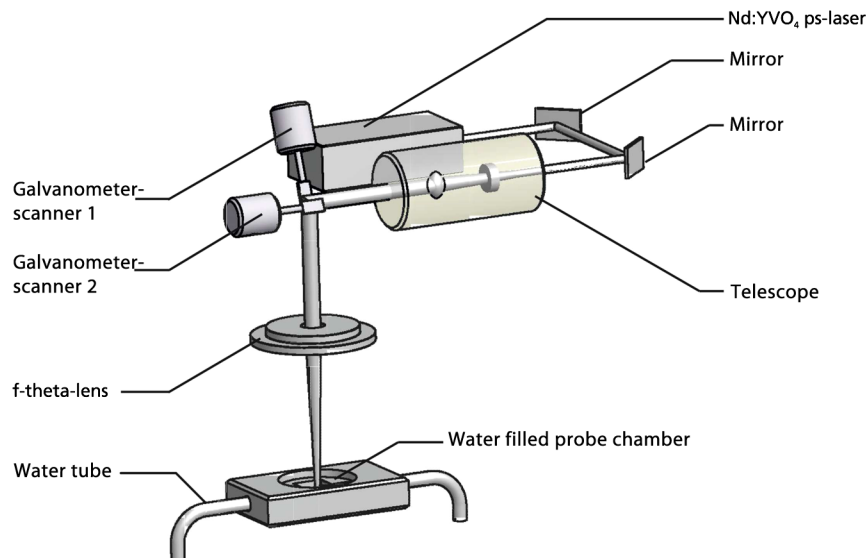


**Fig. 3** Experimental setup comprising a Galilean telescope for focus shifting, a two-dimensional galvanometer-scanner setup, an f-theta focusing lens, and a water-filled sample chamber.

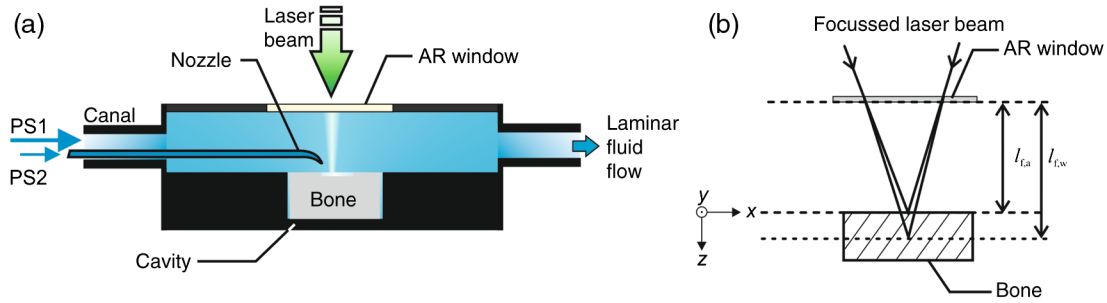


**Fig. 4** (a) The water-filled sample chamber contains two pump systems, PS1 and PS2, which provide a water flow in the chamber and on the tissue surface. The laser beam is scanned by galvanometer scanners in the  $xy$ -plane to generate rectangular incisions with 4-mm length (fast  $x$ -axis) and 0.1 to 1.5 mm width (slow  $y$ -axis). (b) Due to refraction in the water the focal plane is shifted into the bone. The distance of the focal plane from the entrance window  $l_{f,a}$  is increased to  $l_{f,w}$  when the sample chamber is filled with water.

times the threshold fluence  $F_{\text{thr}} = 0.45 \text{ J/cm}^2$ . The focus of the beam was scanned by the galvanometer scanners in a rectangular raster scan pattern with a length of  $L_x = 4 \text{ mm}$  and a width of  $L_y = 0.5 \text{ mm}$  and a line distance of  $\Delta L_y = 100 \mu\text{m}$  as shown in Fig. 2(a). The fast scan axis is the  $x$ -axis, which is oriented parallel to the water flow direction. The scan speed was set to  $v_{\text{sc}} = 4.8 \text{ m/s}$  for a repetition frequency of  $f_R = 20 \text{ kHz}$ .

For every ablation experiment, the total time to perform the incision was measured. The volume of the incision was measured afterward with an optical coherence tomography (OCT) system developed at Fraunhofer ILT with a total axial scan range of 9 mm, an axial resolution of  $22 \mu\text{m}$ , and a lateral resolution of  $55 \mu\text{m}$ . From the ablated volume  $V$  and the total time  $t$  to generate the incision, the ablation rate  $V/t$  is calculated. To measure the volume, we performed B-Scans in the  $xz$ -plane and the  $yz$ -plane.

The sample chamber is connected to two different pump systems PS1 and PS2. The pump system PS1 flushes the chamber and provides a laminar water flow with an average flow speed of  $0.08 \text{ m/s}$ . Its purpose is to ensure a constant water height above the tissue surface and a constantly water-filled chamber. PS2 provides a turbulent liquid flow from a nozzle with an inner diameter of  $d_n = 1 \text{ mm}$ . The nozzle is directed in a 45-degree angle onto the tissue surface, its purpose is to remove ablation debris and microbubbles from the narrow groove with a high-aspect ratio. We measured and calculated the maximal water

impact force from PS2 to be  $0.1 \text{ N}$  at the maximum flow rate of  $570 \text{ mL/min}$ . This flow rate corresponds to an average flow speed of  $12 \text{ m/s}$  close to the sample surface.

## 5 Results

A raster scan with six lines having a line distance of  $100 \mu\text{m}$  was initiated in the  $xy$ -plane. The length was set to  $4 \text{ mm}$  and the intended groove width was set to  $0.5 \text{ mm}$ . One ablated layer corresponds to one cycle of the raster scan. After each ablated layer, the focus was shifted by  $0.2 \mu\text{m}$  in positive  $z$ -direction. We found that value to be optimal in our previous investigations.<sup>47</sup>

The results of the simulation are shown in Fig. 5. The calculated groove cross section is cone-shaped and the bottom of the groove is not a plane. The calculated groove width at the initial bone surface is  $700 \mu\text{m}$ , this value is  $200 \mu\text{m}$  greater than the set value for the raster scan. The groove shape depends on the pulse overlap in  $y$ -direction. The depth increases finally as a linear function of the number of ablated layers as long as the bottom of the groove still has a plateau. Once the walls of the groove come together, the depth increases as a function of the number of ablated layers slows down to a logarithmic dependence. This is due to the fact that the angle of incidence is now greater than zero for all  $y$ -positions. As illustrated in Fig. 1, the  $y$ -position, at which the threshold is exceeded, shifts toward the center of the groove due to a larger effective spot diameter.

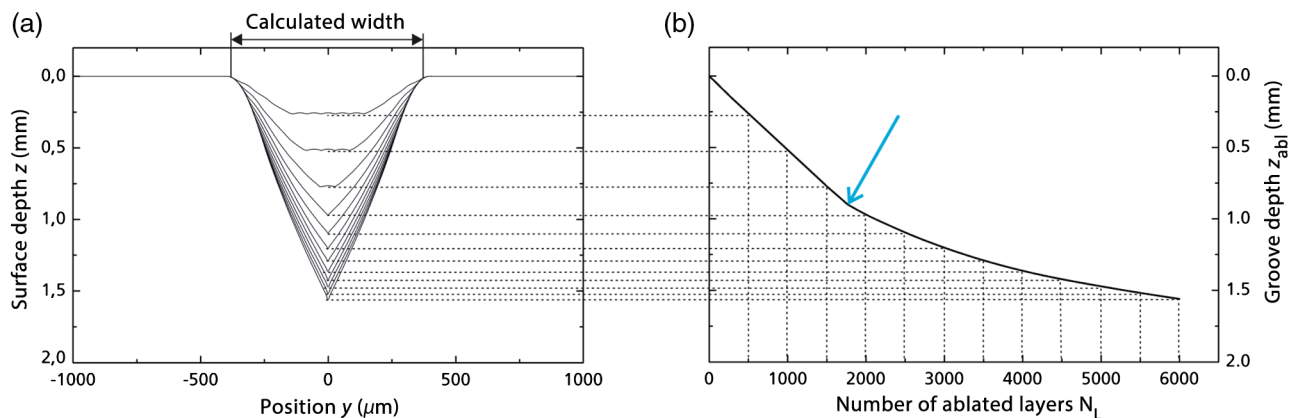


**Fig. 5** (a) Simulation of the cross section of the groove in the  $yz$ -plane and (b) the maximum groove depth  $z_{\text{abl}}$  as a function of the number of ablated layers in steps of 500 ablated layers. The arrow indicates the depth where the linear dependence changes to a logarithmic dependence.

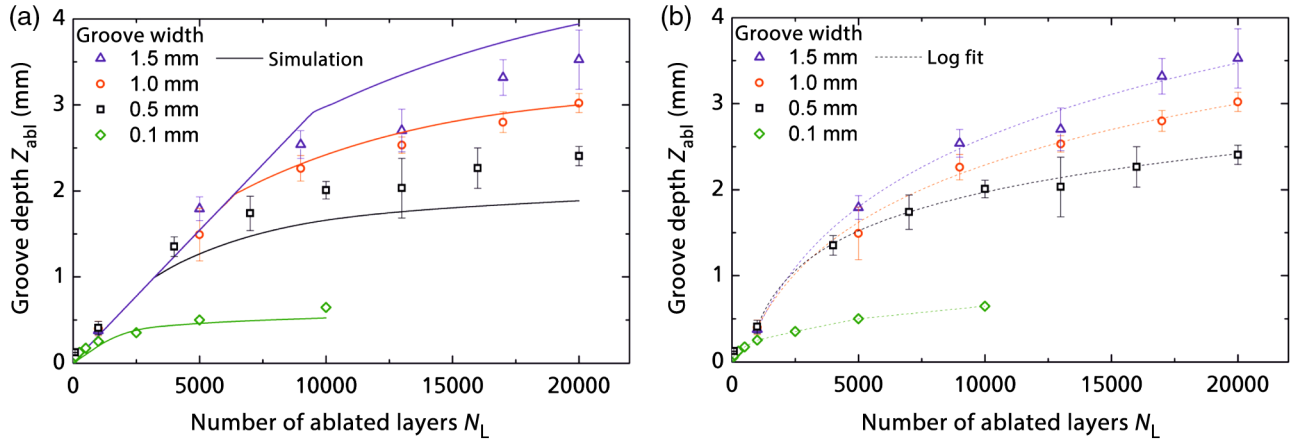


**Fig. 6** (a) Measured and simulated groove depth as a function of the number of ablated layers for different set groove width. (b) A logarithmic fit to the measured data is indicated by the dashed lines.

According to these results, the groove depth depends on the groove width and on the number of lines in the raster scan, since the groove walls come together later for larger groove widths. As shown in Fig. 6(a), we generated incisions with different groove width and measured the groove depth as a function of the number of ablated layers. The groove depth is defined as the  $z$ -position of the bottom of the groove at its deepest point, while the groove width is defined as the width at the initial surface. The groove width increases by increasing the number of lines in the raster scan, while keeping the line distance constant to  $\Delta L_y = 100 \mu\text{m}$ . Each measurement was performed on five different bone samples in order to estimate the standard deviation indicated by the error bars. The solid lines denote the expected groove depth according to the simulation.

In Fig. 6(b), a logarithmic fit according to the equation  $Z_{abl} = a + b \ln(N_L + c)$  is indicated by the dotted lines. Here  $a$ ,  $b$ , and  $c$  are the free parameters with the restriction to only positive values for  $b$ . For a logarithmic curve fit, the coefficient of determination is  $R^2 = 0.998 \pm 0.001$ . The free parameters in the simulation were varied in order to maximize  $R^2$ . The

final values are  $\mu = 80 \text{ nm}$  and  $F_{thr} = 0.45 \text{ J/cm}^2$  leading to  $R^2 = 0.979 \pm 0.016$ .

Figure 7 shows cross sectional images—in the  $yz$ -plane—of the grooves. The images were taken with OCT. The OCT images are overlaid with the calculated surface contours in the same scale. While the simulation shows V-shaped grooves, the OCT images reveal steeper sides and a trend to a slight U-shape of the cross section.

For surgical applications, not only the maximum depth of an incision is of importance, but also the time that is necessary to perform an incision. For surgeons, the cutting speed, which depends on the ablated volume per time, is of interest. For this reason, we denote the ablation rate as the total volume of the groove  $V$  divided by the total time  $t$  that is needed to generate that groove. Since the rise of the groove depth slows down with increasing depth the ablation rate drops. Therefore, we measured the ablation rate as a function of the depth. The maximum ablation rate achieved with our laser system amounts to  $V/t = (0.19 \pm 0.015) \text{ mm}^3/\text{s}$  for a depth of 0.12 mm, while it drops to  $(0.013 \pm 7.5 \cdot 10^{-4}) \text{ mm}^3/\text{s}$  for 3-mm deep incisions, see Fig. 8.

To enable different research groups to compare their results for the ablation rate or ablation efficiency, a consistent definition of the ablation rate is needed. In the literature, no uniform definition of the ablation rate or ablation efficiency exists. The most common target parameters in the above-cited articles are the

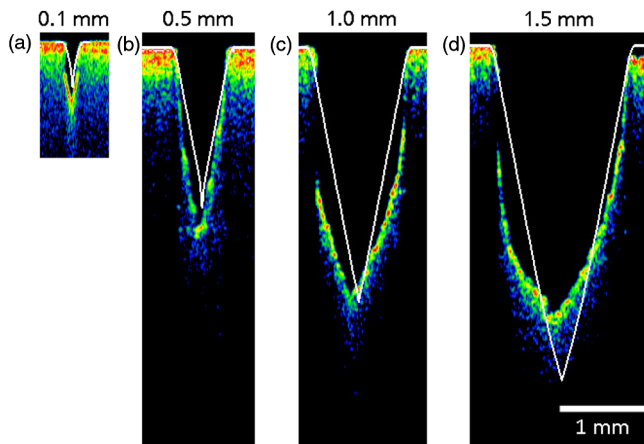


**Fig. 7** Optical coherence tomography (OCT) images and simulation of the cross section ( $yz$ -plane) of the grooves of different widths for a number of ablated layers of (a)  $N_L = 10,000$  and (b)–(d)  $N_L = 20,000$ . The OCT signal intensity is indicated by different colors. The solid white lines show the simulated groove shape. All images (a)–(d) have the same scale.

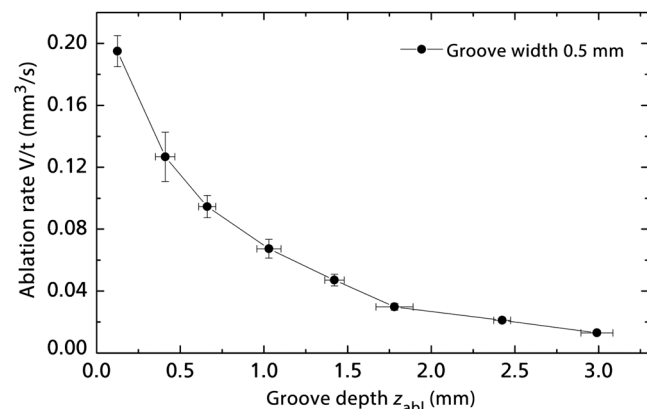


**Fig. 8** Ablation rate as a function of the depth for a groove width of 0.5 mm. The solid line is a guide to the eye.

**Table 1** Ablation rate according to different definitions. The relative standard deviation of the values from our publication is ~5%. The result corresponds to the datapoint at 78 layers of the groove width 0.5 mm from Fig. 8.

Parameter	Symbol	Unit	Values		
			This paper	Ref. 18 (Er:YAG)	Ref. 19 (CO <sub>2</sub> )
Pulse energy	$E_p$	mJ	1	72.5	78
Pulse duration	$t_p$	s	$25 \times 10^{-12}$	$250 \times 10^{-6}$	$80 \times 10^{-6}$
Average power	$P$	W	20	14.5	46.2
Ablation rate	$V/t$	mm <sup>3</sup> /s	0.19	1.47	3.4
Ablated volume per pulse	$V_p$	μm <sup>3</sup>	9500		
Ablated depth per layer	$Z_L$	μm	1.58	500	
Specific energy	$\eta$	J/mm <sup>3</sup>	105	8.2	13.61 <sup>a</sup>
Ablation efficiency	$1/\eta$	mm <sup>3</sup> /J	$9.5 \cdot 10^{-3}$	0.122 <sup>a</sup>	0.073

<sup>a</sup>The value given in the cited reference. From this value, the ablation rate  $V/t$  was calculated.

depth per pulse given in μm, the ablated volume per pulse or mass per pulse in mm<sup>3</sup> or μg, the specific energy  $\eta$  in J/mm<sup>3</sup>, respectively, its reciprocal and sometimes the ablated mass per energy in μg/J. These parameters can only be converted one to another if further parameters are given in the respective publication, such as the scanning speed, repetition rate of the laser, pulse energy, and ablated volume. Hence, sometimes it is not possible to compare different results of the ablation rate, especially when the depth per pulse is given without knowledge of the pulse overlap or the ablated volume per pulse. To make our results comparable to most of the other publications from this field of research, we calculated the ablation rate according to five different definitions. Table 1 lists the ablation rate achieved in this work in comparison with the highest ablation rate for bone tissue that was achieved up to now with Er:YAG<sup>18</sup> and CO<sub>2</sub> lasers.<sup>19</sup>

Microscope and scanning electron microscope images published in our previous paper showed no evidence of thermal damage or side effects like micro-cracks to surrounding tissue.<sup>47</sup>

## 6 Discussion and Outlook

During a laser pulse, a so-called skin-layer is formed with electron densities in the order of  $10^{21} \text{ cm}^{-1}$ .<sup>48</sup> That leads to significant increase of the absorption coefficient to values similar of those in metals. Based on our simulations, we found values for the skin-layer depth of  $\mu = 80 \text{ nm}$  and a threshold fluence of  $F_{\text{thr}} = 0.45 \text{ J/cm}^2$ , very similar to the values calculated by Nolte et al.<sup>36</sup> for USPL ablation of metals. The skin-layer thickness corresponds to the optical penetration depth. According to Feit et al.,<sup>48</sup> for an increase of the pulse energy, transmission and absorption saturate and only the reflection at the skin layer increases. The low-penetration depth, which cannot be overcome with increasing pulse energy, leads to limitations of the ablation efficiency; for that reason, working at 2.5 to 5 times the ablation threshold leads to the most efficient ablation.<sup>37</sup> Additionally, plasma shielding can occur at pulse energies above the threshold. These issues are principal limitations of the plasma-mediated ablation. That is the reason for the low ablation rate compared to the thermal ablation based on the vaporization

of water. We found a specific ablation enthalpy of  $105 \text{ J/mm}^3$ . This value is 40 times higher than the vaporization enthalpy of water.

A limitation of the incision aspect ratio (depth/width) to a value of about 3 is obvious from our simulation and experiments. The main reason is the Gaussian beam profile in connection with angle-dependent reflection at the incision walls. Steeper incision walls and higher aspect ratios should be achieved with top-hat beam profiles.

According to the simulations, the groove shape should be symmetrical, but the OCT measurements reveal asymmetric cross sections. Possible reasons are: (a) the inhomogeneity of the tissue samples, which leads to statistical deviations of the optical properties and tensile strength, (b) the turbulent water flow, and (c) an asymmetric debris removal from the bottom of the groove due to an imperfect alignment of the nozzle.

The used model assumes that the debris is totally removed from the interaction area before the next laser pulse is applied. Furthermore, we assumed that for every laser pulse, an approximately undisturbed local environment close to the interaction region persists. The validity can be checked as follows. With a scan speed of 4.8 m/s, the pulse distance of two pulses at  $f_R = 20 \text{ kHz}$  is  $240 \mu\text{m}$ . The water exchange time for 12 m/s flow speed within this distance is 2.5 times smaller than the time between two laser pulses  $\Delta t = 50 \mu\text{s}$  at 20 kHz. Moreover, compared to the pulse distance the thermal penetration depth  $z_{\text{therm}} = 2\sqrt{\kappa\Delta t} = 6 \mu\text{m}$ , with  $\kappa = 1.7 \text{ m}^2/\text{s}$ ,<sup>44</sup> is negligible.

Another influencing factor is the plasma-induced cavitation, which can enhance the ablation by additional jet-induced debris removal, but can also hinder ablation by distorting the laser focus for a subsequent laser pulse. The latter effect can occur under the condition that the bubble size is larger than the pulse distance and the bubble oscillation time is larger than the inverse laser repetition frequency. Bubble size and lifetime can be estimated using the relations given by Refs. 31 and 49. For a 1-mJ laser pulse with 30-ps duration, the bubble oscillation time in water close to a solid boundary is 140 to 150 μs with a lifetime of about 300 μs. The maximum bubble radius for this pulse energy is about 750 μm. Hence, the bubble expansion

velocity is 10 m/s. This value is only slightly below the value of the water flow velocity of 12 m/s near the surface. The bubbles can potentially influence the energy deposition during a 20-kHz laser pulse series with 240- $\mu\text{m}$  pulse distance, in particular, if the scan direction is the same as the water flow direction. In the raster a scan, as shown in Fig. 2(a), this would be the case for every second line number.

Despite the influences of the cavitation bubbles and the principle limitations of the plasma-mediated ablation, the ablation rates achieved with USPL can be enhanced by a factor of ten to values similar to those of Er:YAG lasers. For this purpose, a laser system with a repetition frequency up to 200 kHz with constant pulse energy of 1 mJ should be used in connection with a scanning speed of at least 50 m/s. The newest developments of USPL technology<sup>46</sup> are promising in this context.

## 7 Conclusion

We presented the plasma-mediated ablation of cortical bone tissue with ps-laser radiation at 532 nm and 1 mJ pulse energy. Water flow rates of up to 570 ml/min were used for debris removal. We simulated the incision depth and cross sectional shape for macroscopic incisions with a depth up to 3.5 mm and a width up to 1.5 mm. The highest ablation rate achieved is 0.19 mm<sup>3</sup>/s for a depth of 0.12 mm. This is up to now the highest value for ablation of hard tissue with USPL, but still one order of magnitude lower than the ablation rates achieved with Er:YAG or CO<sub>2</sub> lasers. In our experiments, we observed no thermal damage of the tissue, but histological investigations must still be performed for a concluding statement about the tissue damage.

## References

1. T. E. Gordon, "Some effects of laser impacts on extracted teeth," *J. Dent. Res.* **45**(2), 372–375 (1966).
2. S. D. Gertzbein et al., "The effect of laser osteotomy on bone healing," *Laser Surg. Med.* **1**(4), 361–373 (1981).
3. A. A. Serafetinides et al., "Picosecond laser ablation of dentine in endodontics," *Lasers Med. Sci.* **14**(3), 168–174 (1999).
4. R. F. Z. Lizarelli et al., "Characterization of enamel and dentin response to Nd:YAG picosecond laser ablation," *J. Clin. Laser Med. Sur.* **17**(3), 127–131 (1999).
5. R. Hibst and U. Keller, "Experimental studies of the application of the Er:YAG laser on dental hard substances: 1. measurement of the ablation rate," *Laser Surg. Med.* **9**(4), 338–344 (1989).
6. J. Youn, P. Sweet, and G. M. Peavy, "A comparison of mass removal, thermal injury, and crater morphology of cortical bone ablation using wavelengths 2.79, 2.9, 6.1, and 6.45  $\mu\text{m}$ ," *Laser Surg. Med.* **39**(4), 332–340 (2007).
7. B. M. Kim et al., "Influence of pulse duration on ultrashort laser pulse ablation of biological tissues," *J. Biomed. Opt.* **6**(3), 332–338 (2001).
8. M. Werner et al., "CO<sub>2</sub> laser milling of hard tissue," *Proc. SPIE* **6435**, 64350E (2007).
9. R. G. McCaughey et al., "Femtosecond laser ablation of the stapes," *J. Biomed. Opt.* **14**(2), 024040 (2009).
10. M. H. Niemz, "Investigation and spectral analysis of the plasma-induced ablation mechanism of dental hydroxyapatite," *Appl. Phys. B* **58**(4), 273–281 (1994).
11. A. Baraba et al., "Ablative potential of the erbium-doped yttrium aluminium garnet laser and conventional handpieces: a comparative study," *Photomed. Laser Surg.* **27**(6), 921–927 (2009).
12. E. Stein et al., "Acute and chronic effects of bone ablation with a pulsed holmium laser," *Laser Surg. Med.* **10**(4), 384–388 (1990).
13. A. V. Rode et al., "Subpicosecond laser ablation of dental enamel," *J. Appl. Phys.* **92**(4), 2153–2158 (2002).
14. M. Mehrwald et al., "Analysis of the short-pulsed CO<sub>2</sub> laser ablation process for optimizing the processing performance for cutting bony tissue," *Proc. SPIE* **7562**, 75620P (2010).
15. M. S. Bello-Silva et al., "Precise ablation of dental hard tissues with ultra-short pulsed lasers. Preliminary exploratory investigation on adequate laser parameters," *Lasers Med. Sci.* **28**(1), 171–184 (2012).
16. F. Schelle et al., "Ultrashort pulsed laser (USPL) application in dentistry: basic investigations of ablation rates and thresholds on oral hard tissue and restorative materials," *Lasers Med. Sci.* **29**(6), 1775–1783 (2013).
17. P. Spencer et al., "Effective laser ablation of bone based on the absorption characteristics of water and proteins," *J. Periodontol.* **70**(1), 68–74 (1999).
18. K. Stock et al., "Efficient bone cutting with the novel diode pumped Er:YAG laser system: *in vitro* investigation and optimization of the treatment parameters," *Proc. SPIE* **8926**, 89263P (2014).
19. M. Werner et al., "CO<sub>2</sub> laser free-form processing of hard tissue," *Proc SPIE* **6632**, 663202 (2007).
20. N. Jowett et al., "Bone ablation without thermal or acoustic mechanical injury via a novel picosecond infrared laser (PIRL)," *Otolaryngol. Head Neck Surg.* **150**(3), 385–393 (2014).
21. K. Stock et al., "Primary investigations on the potential of a novel diode pumped Er:YAG laser system for bone surgery," *Proc. SPIE* **8565**, 85656D (2013).
22. X. Zhang et al., "Influence of water layer thickness on hard tissue ablation with pulsed CO<sub>2</sub> laser," *J. Biomed. Opt.* **17**(3), 038003 (2012).
23. A. E. Pichahchy, D. A. Cremers, and M. J. Ferris, "Elemental analysis of metals under water using laser-induced breakdown spectroscopy," *Spectrochim. Acta B* **52**(1), 25–39 (1997).
24. J. Lu et al., "Mechanisms of laser drilling of metal plates underwater," *J. Appl. Phys.* **95**(8), 3890–3894 (2004).
25. H. P. Berlien and G. J. Müller, *Applied Laser Medicine*, Springer, New York (2003).
26. J. Kuttenger et al., "Bone healing of the sheep tibia shaft after carbon dioxide laser osteotomy: histological results," *Lasers Med. Sci.* **25**(2), 239–249 (2010).
27. M. H. Niemz, *Laser-Tissue Interactions*, Springer, Heidelberg (2004).
28. D. D. Lo et al., "Femtosecond plasma-mediated laser ablation has advantages over mechanical osteotomy of cranial bone," *Laser Surg. Med.* **44**(10), 805–814 (2012).
29. F. de Assis et al., "Influence of the hydration state on the ultrashort laser ablation of dental hard tissues," *Lasers Med. Sci.* **28**(1), 215–222 (2013).
30. A. Vogel, "Nonlinear absorption: intraocular microsurgery and laser lithotripsy," *Phys. Med. Biol.* **42**(5), 895–912 (1997).
31. J. Noack and A. Vogel, "Energy balance of optical breakdown in water at nanosecond to femtosecond time scales," *Appl. Phys. B* **68**(2), 271–280 (1999).
32. G. M. Hale and M. R. Querry, "Optical constants of water in the 200-nm to 200-mm wavelength region," *Appl. Opt.* **12**(3), 555–563 (1973).
33. D. Meschede, *Optics Light and Lasers*, 3rd ed., pp. 504–527, Vieweg, Wiesbaden (2008).
34. B. Richerzhagen, G. Delacretaz, and R. P. Salathe, "Complete model to simulate the thermal defocusing of a laser beam focused in water," *Opt. Eng.* **35**(7), 2058–2066 (1996).
35. E. G. Gamaly et al., "Ablation of solids by femtosecond lasers: ablation mechanism and ablation thresholds for metals and dielectrics," *Phys. Plasmas* **9**(3), 949–957 (2002).
36. S. Nolte et al., "Ablation of metals by ultrashort laser pulses," *J. Opt. Soc. Am. B* **14**(10), 2716–2722 (1997).
37. A. Vogel and V. Venugopalan, "Mechanisms of pulsed laser ablation of biological tissues," *Chem. Rev.* **103**(2), 577–644 (2003).
38. J. Noack and A. Vogel, "Laser-induced plasma formation in water at nanosecond to femtosecond time scales: calculation of thresholds, absorption coefficients, and energy density," *J. Quantum Electron.* **35**(8), 1156–1167 (1999).
39. A. Vogel, *Lasers in Ophthalmology—Basic, Diagnostic and Surgical Aspects*, pp. 99–113, Kugler Publications, Den Haag, Netherlands (2003).
40. K. Nahen and A. Vogel, "Plasma formation in water by picosecond and nanosecond Nd:YAG laser pulses—Part II: transmission, scattering, and reflection," *IEEE J. Sel. Top. Quantum Electron.* **2**(4), 861–871 (1996).

41. A. J. Welch and M. J. C. van Gemert, *Optical and Thermal Response of Laser-Irradiated Tissue*, Plenum Press, New York (1995).
42. T. F. Deutsch and M. W. Geis, "Self-developing UV photoresist using excimer laser exposure," *J. Appl. Phys.* **54**(12), 7201–7204 (1983).
43. N. Ugryumova, S. J. Matcher, and D. P. Attenburrow, "Measurement of bone mineral density via light scattering," *Phys. Med. Biol.* **49**(3), 469–483 (2004).
44. F. A. Duck, *Physical Properties of Tissue, A Comprehensive Reference Book*, IPPEM, New York (2012).
45. B. Emigh et al., "Porcine cortical bone ablation by ultrashort pulsed laser irradiation," *J. Biomed. Opt.* **17**(2), 028001 (2012).
46. P. Russbueltd et al., "Innoslab amplifiers," *IEEE J. Sel. Top. Quantum Electron.* **21**(1), 31001-31017.
47. C. Tulea et al., "Highly efficient nonthermal ablation of bone under bulk water with a frequency-doubled Nd:YVO<sub>4</sub> picosecond laser," *Proc. SPIE* **8565**, 85656E (2013).
48. M. D. Feit, A. M. Komashko, and A. M. Rubenchik, "Ultra-short pulse laser interaction with transparent dielectrics," *Appl. Phys. A* **79**(7), 1657–1661 (2004).
49. A. Vogel, W. Lauterborn, and R. Timm, "Optical and acoustic investigations of the dynamics of laser-produced cavitation bubbles near a solid boundary," *J. Fluid Mech.* **206**, 299–338 (1989).

**Cristian-Alexander Tulea** is a PhD student at the RWTH Aachen University and a research associate at Fraunhofer Institute for Laser Technology ILT in Aachen, Germany. He received his diploma degree in physics from the University of Bonn for the development of a continuous wave optical parametric oscillator in the terahertz range. His current research topics include the investigation of hard tissue ablation and the development of miniaturized laser scanners for hand guided laser therapy.

Biographies for the other authors are not available.